A hybrid approach for analysis of a beam-soil structure under a moving random load

L.T. Si [a], Y. Zhao [a, *], Y. H. Zhang [a], D. Kennedy [b]

[a] *State Key Laboratory of Structural Analysis for Industrial Equipment, Faculty of Vehicle Engineering and Mechanics, Dalian University of Technology, Dalian 116023, PR China*

[b] *Cardiff School of Engineering, Cardiff University, Cardiff CF24 3AA, Wales, UK*

Abstract

To study the stochastic response of a beam-soil structure under a moving random load, a hybrid method based on the pseudo-excitation method and the wavelet method is proposed. By means of the pseudo-excitation method, the non-stationary random vibration analysis is transformed into a conventional moving harmonic load problem. Analytical solutions of the power spectral density and standard deviation of vertical displacement are derived in an integral form. However, the integrand is singular and highly oscillatory, and computational time is an important consideration because a large number of frequency points must be computed. To calculate the response accurately and efficiently, a wavelet approach is introduced. Numerical results show that the frequency band which brings the most significant response is dependent on the load velocity. The hybrid method provides a useful tool to estimate the ground vibration caused by traffic loads.

Keywords: moving random load; pseudo-excitation method; Fourier transform; wavelet method

1. Introduction

Trains travelling at speed present moving loads which are known to excite large amplitude, wide frequency spectrum vibration in the track which can propagate over a long distance. Such vibration can enter buildings via the foundations and affect the working of sensitive equipment and human comfort. The moving loads are random in

* *Corresponding author. Tel: +86 411 8470 6337; Fax:+86 411 8470 6337; E-mail address: yzhao@dlut.edu.cn*

nature, for example due to rail irregularities.

Much research has already been done to solve the deterministic problems of a half-space subjected to moving loads. The models are becoming complicated and various solution methods have emerged. Lamb [1] first proposed the problem of an elastic medium subjected to an impulsive force. Eason [2] extended the problem by considering a moving force acting on a uniform half-space. Gakenheimer and Miklowitz [3] derived the transient displacements inside the half-space induced by a moving load, while Fryba [4] analyzed the steady-state response of an unbounded elastic half-space under a moving load. They all considered the effect of the velocity of the moving load on the response, and studied the subcritical, critical and supercritical cases. In later studies, a uniform or layered half-space was subjected to different kinds of moving loads including elastically distributed loads [5-7], normal or shear stresses [8], harmonic rectangular [9, 10] or strip loads [11, 12] and vehicle loads [13]. Using a layered half-space model coupled with a track structure subjected to a fixed or moving harmonic load, Sheng et al [14-16] investigated the propagation of vibration theoretically.

However, in actual rail transportation systems, the moving loads caused by vehicles are somewhat stochastic due to the track irregularity and other uncertainties, so that the vibration at any specific ground location is a non-stationary random process. Hunt [17, 18] computed the power spectrum of ground vibration under traffic loads by assuming the ground vibration was a random and statistically stationary process. Sun and Greenberg [19] presented a generalized method to solve the problem of a linear system subjected to moving sources. Metrikine and Vrouwenvelder [20] studied the steady-state surface ground vibration under a point load moving along a beam embedded in a layer, in which a stationary random load was investigated, with the randomness represented by a uniformly distributed phase angle. Sheng et al. [21] investigated ground vibration considering vertical track irregularities, but the power spectral density (PSD) was not time-varying because the fast Fourier transform with respect to time was applied. By using the pseudo-excitation method (PEM), Lu et al. [22] adopted a model similar to Sheng's to study the random response due to random

moving loads in the subcritical case. Considering the PSD of the track irregularity, Lombaert and Degrande [23] studied the random response of a track-soil system under dynamic excitation in the subcritical case.

Much work remains to solve the problems of a beam-soil structure under random moving loads, especially in the critical and supercritical cases. It is time consuming to obtain the second-order statistics of the response by traditional methods, and the highly oscillatory nature of the integrand can cause large errors in the numerical results. The objective of this paper is to present a convenient method to study the non-stationary stochastic vibration of a beam-soil structure subjected to a moving random load. A hybrid method based on the PEM and wavelet method is proposed. In section 2, the basic model and governing equations are provided. In section 3, the PEM used in a linear system is introduced. An analytical solution is given in section 4 and the wavelet approach to compute the integrands is shown in section 5. Sections 6 and 7 give numerical results, discussion and conclusions.

2. Model and governing equations

Figure 1 depicts a beam-soil structure consisting of an infinitely long beam located on the surface of a homogenous isotropic visco-elastic half-space and subjected to a random load $p(t)$ moving with velocity V.

The vertical motion of the beam is described by the Euler-Bernoulli equation

$$EI\frac{\partial^4 W(x,t)}{\partial x^4}+\rho_B\frac{\partial^2 W(x,t)}{\partial t^2}=p(t)\delta(x-Vt)-a\sigma_{zz}(x,0^+,t) \tag{1}$$

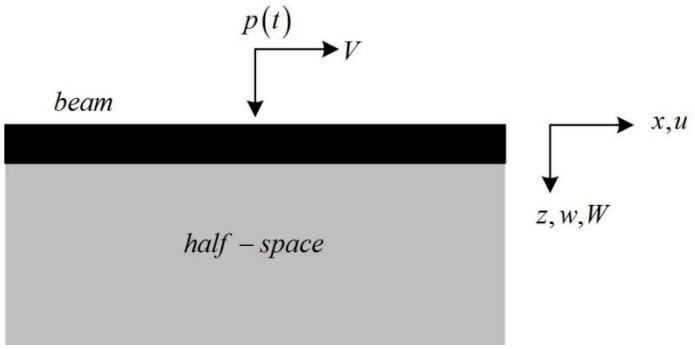

Figure 1. Beam-soil structure under a moving random load.

where $W(x,t)$ is the vertical displacement of the beam, $\sigma_{zz}(x,z,t)$ is the vertical stress, EI and ρ_B are the bending stiffness and mass per unit length of the beam, a is its thickness in the y direction and $\delta(\cdot)$ is the Dirac delta function.

By considering a small viscosity in the soil, its motion is modeled by the elastodynamic Navier's equation

$$\left(\hat{\lambda}+\hat{\mu}\right)\nabla_{xz}(\nabla_{xz}\cdot\mathbf{u})+\hat{\mu}\nabla_{xz}^2\mathbf{u}=\rho\frac{\partial^2\mathbf{u}}{\partial t^2} \tag{2}$$

where $\hat{\lambda}=\lambda+\lambda^*\,\partial/\partial t$ and $\hat{\mu}=\mu+\mu^*\,\partial/\partial t$ describe the visco-elastic behavior of the soil, λ and μ are Lamé constants derived from its elastic modulus E and Poisson's ratio ν , λ^* and μ^* are visco-elastic constants, ρ is the mass density of the soil, and $\mathbf{u}(x,z,t)=\{u(x,z,t),w(x,z,t)\}^T$is the time-dependent displacement vector.

It is assumed that the beam does not move horizontally and that the displacements of the beam and the soil are the same at the interfaces. So the boundary and continuity conditions can be written as

$$u(x,0,t)=0 \qquad w(x,0,t)=W(x,t) \tag{3a}$$

$$\lim_{z\to\infty}u(x,z,t)=0 \qquad \lim_{z\to\infty}w(x,z,t)=0 \tag{3b}$$

3. Non-stationary random vibration analysis by PEM

Lombaert et al. [24] proposed an effective methodology to study the non-stationary free field responses under a moving load with a random amplitude. They also used similar methodology to study the random mechanisms of train-track-soil interaction and to evaluate the response of track-soil system due to track unevenness [23, 25, 26]. In this section, a pseudo-excitation method [27-29] is presented to study the response of a beam-soil structure under a moving random load. Assuming that the forces of train-track interaction possess a random characteristic due to the wheel and track unevenness [30, 31], the moving load abstracted from train-track interaction can be modelled as a stationary random process. Although the excitation source of the beam-soil structure is assumed as a stationary random process, the responses at any specific ground location would be a non-stationary random

process due to the load's moving property [22-24].

A Green's function can be used to characterize the dynamic properties of a linear system. The Green's function $\mathbf{G}(\mathbf{x}, t; \boldsymbol{\xi}, \tau)$ represents the dynamic response at location $\mathbf{x}$ and time t when the system is subjected to a vertical impulse at location $\boldsymbol{\xi}$ and time τ. For a time-independent system, the Green's function degenerates to $\mathbf{G}(\mathbf{x} - \boldsymbol{\xi}, t - \tau)$. Assume that $p(t)$ is a vertical load moving along direction $\mathbf{n}$ at speed V, and $\mathbf{D}$ is the domain occupied by the system. According to the principle of superposition, the displacement of the system can be written as

$$\mathbf{u}(\mathbf{x}, t) = \int_0^t \int_{\mathbf{D}} \mathbf{G}(\mathbf{x} - \boldsymbol{\xi} - \mathbf{n}V\tau, t - \tau) \cdot p(\tau) d\boldsymbol{\xi}\, d\tau \tag{4}$$

Applying an expectation operator $E[\cdot]$ to $\mathbf{u}(\mathbf{x}, t)$ generates its correlation function

$$\begin{aligned} \mathbf{R}_{\mathbf{u}}(\mathbf{x}; t_1, t_2) &= E[\mathbf{u}(\mathbf{x}, t_1)\mathbf{u}^{\mathrm{T}}(\mathbf{x}, t_2)] \\ &= \int_0^{t_1} \int_0^{t_2} \mathbf{h}(\mathbf{x}; t_1, \tau_1) \cdot \mathbf{h}^{\mathrm{T}}(\mathbf{x}; t_2, \tau_2) R_p(\Delta\tau) d\tau_1\, d\tau_2 \end{aligned} \tag{5}$$

where

$$\mathbf{h}(\mathbf{x}; t, \tau) = \int_{\mathbf{D}} \mathbf{G}(\mathbf{x} - \boldsymbol{\xi} - \mathbf{n}V\tau, t - \tau) d\boldsymbol{\xi} \tag{6}$$

$\Delta\tau = \tau_2 - \tau_1$ and $R_p(\Delta\tau)$ is the autocorrelation function of the loads. According to the Wiener-Khintchine theorem, the autocorrelation function $R_p(\Delta\tau)$ can be expressed by the PSD $S_p(\omega)$ as

$$E[p(\tau_1)p(\tau_2)] = R_p(\Delta\tau) = \int_{-\infty}^{\infty} S_p(\omega) \mathrm{e}^{\mathrm{i}\omega(\tau_2 - \tau_1)}\, d\omega \tag{7}$$

where $S_p(\omega)$ reflects the energy distribution of a stationary random process in the frequency domain. Substituting Eq. (7) into Eq. (5), the correlation function can be written as

$$\mathbf{R}_{\mathbf{u}}(\mathbf{x}; t_1, t_2) = \int_{-\infty}^{\infty} S_p(\omega) \mathbf{I}^*(\mathbf{x}; \omega, t_1) \mathbf{I}^T(\mathbf{x}; \omega, t_2)\, d\omega \tag{8}$$

$$\mathbf{I}(\mathbf{x}; \omega, t) = \int_0^t \mathbf{h}(\mathbf{x}; t, \tau) \mathrm{e}^{\mathrm{i}\omega\tau} d\tau \tag{9}$$

where the superscript * denotes a complex conjugate.

The time-dependent variance can be obtained by letting $t_1 = t_2 = t$ in Eq. (8):

$$\mathbf{R_u}(\mathbf{x};t) = \sigma_u^2(\mathbf{x};t) = \int_{-\infty}^{\infty} S_p(\omega)\mathbf{I}^*(\mathbf{x};\omega,t)\mathbf{I}^{\mathrm{T}}(\mathbf{x};\omega,t)\,d\omega \tag{10}$$

Here $\sigma_u(\mathbf{x};t)$ is the standard deviation. Obviously, the integrand in Eq. (10) is the PSD of the response, which has a non-stationary property

$$\mathbf{S_u}(\mathbf{x},\omega,t) = S_p(\omega)\mathbf{I}^*(\mathbf{x};\omega,t)\mathbf{I}^{\mathrm{T}}(\mathbf{x};\omega,t) \tag{11}$$

Note that in Eq. (9) $\mathbf{I}(\mathbf{x};\omega,t)$ is the response of the system under a harmonic load $\mathrm{e}^{\mathrm{i}\omega t}$. So if a pseudo-excitation $\tilde{P}(t) = \sqrt{S_p(\omega)}\mathrm{e}^{\mathrm{i}\omega t}$ is applied to the system, the corresponding response evolves to $\tilde{\mathbf{u}}(\mathbf{x};\omega,t) = \sqrt{S_p(\omega)}\mathbf{I}(\mathbf{x};\omega,t)$. Thus the PSD can be obtained easily from

$$\mathbf{S_u}(\mathbf{x},\omega,t) = \tilde{\mathbf{u}}^*(\mathbf{x};\omega,t)\tilde{\mathbf{u}}^{\mathrm{T}}(\mathbf{x};\omega,t) = S_p(\omega)\mathbf{I}^*(\mathbf{x};\omega,t)\mathbf{I}^{\mathrm{T}}(\mathbf{x};\omega,t) \tag{12}$$

Thus the PSD of the random vibration response is now deduced by the PEM.

4. Analytical solution

As shown in section 3, the random response of the system subjected to a random moving load can be directly obtained by applying a pseudo-excitation $\tilde{P}(t) = \sqrt{S_p(\omega)}\mathrm{e}^{\mathrm{i}\omega t}$ to the system. In this section, the PEM is used to solve the problem of a moving stochastic load acting on the beam-soil structure. In addition, the Lamé potentials and Fourier transform method are also introduced. According to the Helmholtz decomposition of a vector field, the solution of Eq. (2) can be expressed, in terms of a scalar potential $\phi = \phi(x;z,t)$ and a vector potential $\boldsymbol{\psi} = [0, -\psi(x;z,t), 0]$, as

$$\mathbf{u} = \nabla\phi + \nabla\times\boldsymbol{\psi} \tag{13}$$

The stress components are expressed simply as

$$\begin{aligned}\sigma_{zz} &= \hat{\lambda}\left(\frac{\partial^2\phi}{\partial x^2} + \frac{\partial^2\phi}{\partial z^2}\right) + 2\hat{\mu}\left(\frac{\partial^2\phi}{\partial z^2} - \frac{\partial^2\psi}{\partial x\,\partial z}\right)\\ \sigma_{zx} &= \hat{\mu}\left(2\frac{\partial^2\phi}{\partial x\,\partial z} - \frac{\partial^2\psi}{\partial x^2} + \frac{\partial^2\psi}{\partial z^2}\right)\end{aligned} \tag{14}$$

Substituting Eq. (14) into Eq. (2) leads to the wave equations

$$\frac{\partial^2\phi}{\partial t^2} - \left(c_{\mathrm{P}}^2 + \frac{\lambda^* + 2\mu^*}{\rho}\frac{\partial}{\partial t}\right)\left(\frac{\partial^2\phi}{\partial x^2} + \frac{\partial^2\phi}{\partial z^2}\right) = 0 \tag{15}$$

$$\frac{\partial^2\psi}{\partial t^2}-\left(c_{\mathrm{S}}^2+\frac{\mu^*}{\rho}\frac{\partial}{\partial t}\right)\left(\frac{\partial^2\psi}{\partial x^2}+\frac{\partial^2\psi}{\partial z^2}\right)=0 \tag{16}$$

where $c_{\mathrm{P}}=\sqrt{(\lambda+2\mu)/\rho}$ and $c_{\mathrm{S}}=\sqrt{\mu/\rho}$ are the velocities of the dilatational waves and the shear waves, respectively.

By applying the Fourier transforms

$$\begin{aligned}\tilde{\tilde{f}}(\theta,\beta)&=\int_{-\infty}^{\infty}\int_{-\infty}^{\infty}f(x,t)\mathrm{e}^{\mathrm{i}(\beta t-\theta x)}\mathrm{d}x\,\mathrm{d}t\\ f(x,t)&=\frac{1}{4\pi^2}\int_{-\infty}^{\infty}\int_{-\infty}^{\infty}\tilde{\tilde{f}}(\theta,\beta)\mathrm{e}^{-\mathrm{i}(\beta t-\theta x)}\mathrm{d}\theta\,\mathrm{d}\beta\end{aligned} \tag{17}$$

the partial differential equations (15) and (16) are transformed into ordinary differential equations

$$\frac{\partial^2\tilde{\tilde{\phi}}}{\partial z^2}-E_{\mathrm{P}}^2\tilde{\tilde{\phi}}=0 \qquad\qquad \frac{\partial^2\tilde{\tilde{\psi}}}{\partial z^2}-E_{\mathrm{S}}^2\tilde{\tilde{\psi}}=0 \tag{18}$$

in which $E_{\mathrm{P}}^2=\theta^2-\beta^2/(c_{\mathrm{P}}^2-\mathrm{i}\beta(\lambda^*+2\mu^*)/\rho)$ and $E_{\mathrm{S}}^2=\theta^2-\beta^2/(c_{\mathrm{S}}^2-\mathrm{i}\beta\mu^*/\rho)$.

The general solutions of Eq. (18) are given as

$$\tilde{\tilde{\phi}}=A(\theta,\beta)\mathrm{e}^{-E_{\mathrm{P}}z} \qquad\qquad \tilde{\tilde{\psi}}=B(\theta,\beta)\mathrm{e}^{-E_{\mathrm{S}}z} \tag{19}$$

Substituting Eq. (19) into the Fourier transforms of Eqs. (13) and (14) and using the interface and boundary conditions, algebraic equations in A and B are obtained as

$$\begin{bmatrix}\mathrm{i}\theta & -E_{\mathrm{S}}\\ 2\tilde{\tilde{\mu}}\theta^2-\rho\beta^2-\gamma E_{\mathrm{P}} & 2\mathrm{i}\theta\tilde{\tilde{\mu}}E_{\mathrm{S}}-\mathrm{i}\theta\gamma\end{bmatrix}\begin{Bmatrix}A\\B\end{Bmatrix}=\frac{1}{a}\begin{Bmatrix}0\\ \int_{-\infty}^{\infty}p(t)\mathrm{e}^{\mathrm{i}(\beta-\theta V)t}dt\end{Bmatrix} \tag{20}$$

where $\gamma=(EI\theta^4-\rho_B\beta^2)/a$ and $\tilde{\tilde{\mu}}=\mu-\mathrm{i}\beta\mu^*$

Given that solutions for A and B can be easily obtained by Cramer's rule, thus if the system is subjected to a pseudo-excitation $\tilde{P}(t)=\sqrt{S_p(\omega)}\mathrm{e}^{\mathrm{i}\omega t}$, the pseudo vertical displacement of the surface is derived as

$$\tilde{\tilde{w}}_{\mathrm{P}}(\theta,0,\beta)=2\pi\sqrt{S_p(\omega)}\tilde{\tilde{w}}_{\mathrm{S}}(\theta,\beta)\delta(\beta+\omega-\theta V) \tag{21}$$

in which

$$\tilde{\tilde{w}}_{\mathrm{S}}(\theta,\beta)=\frac{E_{\mathrm{S}}E_{\mathrm{P}}-\theta^2}{a(\rho\beta^2E_{\mathrm{S}}+\gamma E_{\mathrm{S}}E_{\mathrm{P}}-\gamma\theta^2)} \tag{22}$$

Applying the inverse transform to Eq. (21) gives the solution for the pseudo displacement in the physical domain

$$\begin{aligned}\widetilde{w}(x,0,t) &= \frac{1}{4\pi^2}\int_{-\infty}^{\infty}\int_{-\infty}^{\infty}\widetilde{\widetilde{w}}_{\mathrm{P}}(\theta,0,\beta)\mathrm{e}^{\mathrm{i}\theta x}\mathrm{e}^{-\mathrm{i}\beta t}\mathrm{d}\theta\,\mathrm{d}\beta \\ &= \frac{\sqrt{S_p(f)}\mathrm{e}^{\mathrm{i}2\pi f t}}{2\pi}\int_{-\infty}^{\infty}\widetilde{\widetilde{w}}_{\mathrm{S}}(\theta,\theta V-2\pi f)\mathrm{e}^{\mathrm{i}\theta(x-Vt)}\mathrm{d}\theta\end{aligned} \tag{23}$$

According to the PEM [27-31], the non-stationary PSD and the time-dependent standard deviations of the vertical displacement at the surface are now computed as

$$S_w = \widetilde{w}^* \cdot \widetilde{w} \tag{24}$$

$$\sigma_w^2(t) = \int_{-\infty}^{\infty} S_w(\omega)d\omega = 4\pi\int_0^{\infty} S_w(f)\mathrm{d}f \tag{25}$$

5. Wavelet approach

Section 4 gives analytical solutions, but because they are in integral form it is difficult to obtain accurate numerical results in practical applications. Also, the integrand in Eq. (23) is singular and highly oscillatory, and the integration interval is infinite. Moreover, computational time is an important consideration because a large number of frequency points must be computed. In this section the wavelet approach is introduced, which is very accurate and highly efficient [32-35]. The wavelet approach is not only suitable to solve linear problems [36-39], but is also robust enough to deal with nonlinear problems [40-42]. Here we use the approach of numerical integration related to a beam-soil structure subjected to a moving load presented by Koziol [38-42].

According to the theory of wavelets, the two-scale relations of the scaling and wavelet function are given as

$$\Phi(x) = \sum_{k=0}^{M} p_k \Phi(2x-k) \tag{26}$$

$$\Psi(x) = \sum_{k=0}^{M} q_k \Phi(2x-k) \tag{27}$$

in which M is an integer characterizing both the accuracy of the scaling function $\Phi(x)$ and the wavelet function $\Psi(x)$, and p_k, q_k are filter coefficients.

The scaling function and wavelet function in the transform domain can be

deduced by setting $\tilde{\tilde{\Phi}}(0) = 1$ and applying the recursive relation [32, 38]

$$\tilde{\tilde{\Phi}}(\theta) = P\left(\mathrm{e}^{-\mathrm{i}\frac{\theta}{2}}\right)\tilde{\tilde{\Phi}}\left(\frac{\theta}{2}\right) = P\left(\mathrm{e}^{-\mathrm{i}\frac{\theta}{2}}\right)P\left(\mathrm{e}^{-\mathrm{i}\frac{\theta}{4}}\right)\tilde{\tilde{\Phi}}\left(\frac{\theta}{4}\right) = \cdots = \prod_{k=1}^{\infty} P\left(\mathrm{e}^{-\mathrm{i}\theta 2^{-k}}\right) \quad (28)$$

$$\tilde{\tilde{\Psi}}(\theta) = Q\left(\mathrm{e}^{-\mathrm{i}\frac{\theta}{2}}\right)\prod_{k=1}^{\infty} P\left(\mathrm{e}^{-\mathrm{i}\theta 2^{-k-1}}\right) \quad (29)$$

where the polynomials P and Q are given as

$$P(z) = \frac{1}{2}\sum_{k=0}^{M} p_k z^k \qquad Q(z) = \frac{1}{2}\sum_{k=0}^{M} q_k z^k \quad (30)$$

In Eqs. (28) and (29), the function $\tilde{\tilde{\Phi}}(\theta)$ denotes a low pass filter and $\tilde{\tilde{\Psi}}(\theta)$ denotes a high pass filter.

Any function $f(x) \in L^2(R)$ can be expanded as

$$f(x) = P_n f(x) + \sum_{j=n}^{\infty} Q_j f(x) = \sum_{k=-\infty}^{\infty} c_{n,k}\Phi_{n,k}(x) + \sum_{j=n}^{\infty}\sum_{k=-\infty}^{\infty} d_{j,k}\Psi_{j,k}(x) \quad (31)$$

in terms of projection operators P_n and Q_j [32, 33, 38] in which $\Phi_{n,k}$ and $\Psi_{j,k}$ are generated from Φ and Ψ by dilation and translation

$$\Phi_{n,k}(x) = 2^{n/2}\Phi(2^n x - k) \quad (32)$$

$$\Psi_{j,k}(x) = 2^{j/2}\Psi\left(2^j x - k\right) \quad (33)$$

Now according to Eq. (31), the Fourier transform of $f(x)$ can also be expanded as the series summation

$$\tilde{\tilde{f}}(\theta) = \sum_{k=-\infty}^{\infty} 2^{n/2} c_{n,k}\Phi(2^n\theta - k) + \sum_{j=n}^{\infty}\sum_{k=-\infty}^{\infty} 2^{j/2} d_{j,k}\Psi\left(2^j\theta - k\right) \quad (34)$$

Noting that $f(x) = (1/2\pi)\int_{-\infty}^{\infty}\tilde{\tilde{f}}(\theta)\mathrm{e}^{\mathrm{i}\theta x}d\theta$, the inverse Fourier transformation of Eq. (34) gives

$$\begin{aligned} f(x) = \left(\frac{2^{-n/2}}{2\pi}\right)\tilde{\tilde{\Phi}}(-x/2^n)\sum_{k=-\infty}^{\infty} c_{n,k}\mathrm{e}^{\mathrm{i}kx/2^n} \\ + \frac{1}{2\pi}\sum_{j=n}^{\infty} 2^{-j/2}\tilde{\tilde{\Psi}}\left(-x/2^j\right)\sum_{k=-\infty}^{\infty} d_{j,k}\mathrm{e}^{\mathrm{i}kx/2^n} \end{aligned} \quad (35)$$

Usually the coefficients $c_{n,k}$ and $d_{j,k}$ are difficult to determine, but for practical

applications one can calculate their analytical approximations in the case of coiflets [32, 34, 38]. Using Eqs. (28) and (29) and characteristics of the coiflets [32, 38, 40], the approximations of the coefficients can be computed as

$$c_{n,k} = \int_{-\infty}^{\infty} f(x)\Phi_{n,k}(x)dx \approx 2^{-n/2} f\big((k + M_1)2^{-n}\big) \tag{36}$$

$$\begin{aligned} d_{j,k} &= \int_{-\infty}^{\infty} f(x)\Psi_{j,k}(x)dx \\ &\approx 2^{-j/2-1} \sum_{m=0}^{M} (-1)^m p_{3N-1-m} f\left((M_1 + m + 2k)2^{-j-1}\right) \end{aligned} \tag{37}$$

in which $M_1 = \sum_{k=0}^{M} \frac{1}{2} k p_k$ and $M = 3N - 1$

By simplification, Eq. (35) can be approximated as

$$\begin{aligned} f(x) &= \lim_{n\to\infty} \frac{2^{-n-1}}{\pi} \\ &\prod_{j=1}^{k_p} \left(\sum_{k=0}^{M} \frac{1}{2} p_k \mathrm{e}^{\mathrm{i}kx2^{-j-n}} \right) \sum_{s=s_{min}}^{s_{max}} \tilde{f}\big((s + M_1)2^{-n}\big) \mathrm{e}^{\mathrm{i}sx/2^n} \end{aligned} \tag{38}$$

where k_p is an integer whose value depends on the accuracy demanded. The summation of s from $s_{min} = \theta_{min}2^n - 16$ to $s_{max} = \theta_{max}2^n - 1$ is determined by the interval $[\theta_{min}, \theta_{max}]$ and must cover the range of variable θ which influences the original function. In the numerical calculations, the low pass coiflet filter coefficients p_k are listed in the Appendix, and the range of variable θ is chosen to be $[-2, 2]$ for consistency with the other parameters $M = 17$, $M_1 = 7$, $k_p = 10$.

Theoretically speaking, increasing n leads to more precise results but requires more computation time. Numerical simulations show that for $n > 16$ the approximation in Eq. (38) does not change significantly. So $n = 17$ yields a good balance between accuracy and economy.

6. Numerical example and discussion

The objective of this paper is to present an effective method to deal with random moving load problems and to calculate the response economically. A flow chart of the present method is shown in Figure 2.

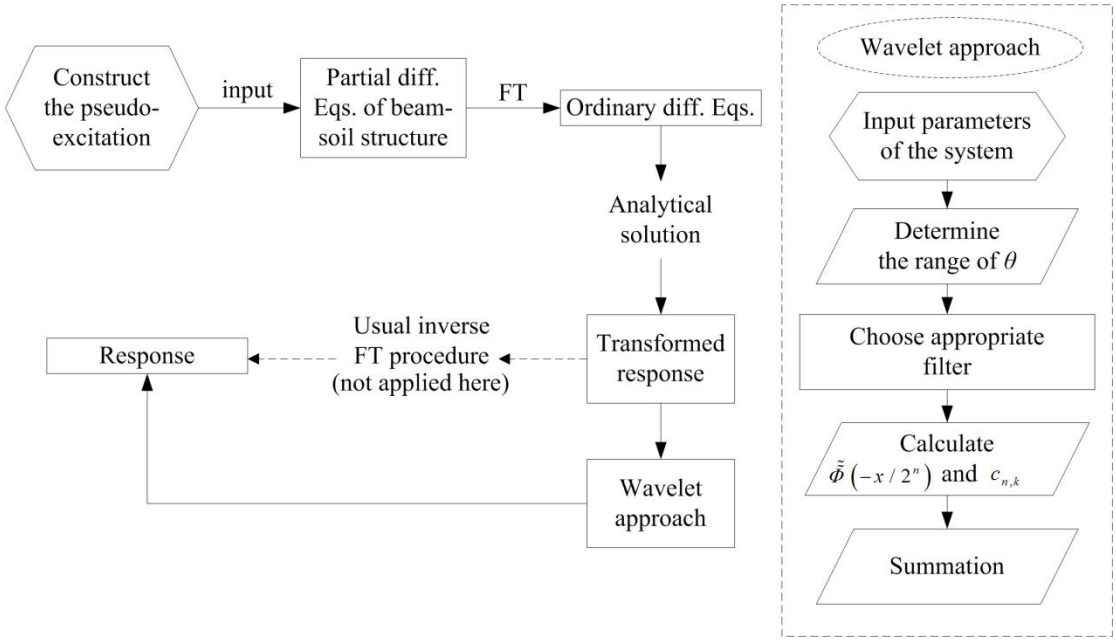

Figure 2. Flow chart of the hybrid method.

Table 1 gives the parameters of the system under consideration, which were previously used in [20, 39]. It is worth mentioning that the soil is so soft that modern trains can easily exceed its Rayleigh wave velocity (75.86 m s^{-1}). Without loss of generality, all responses are calculated at the origin (0, 0), and a simple band-limited white noise is taken to represent the PSD of the moving load:

Table 1

Parameters of the system

Soil	Lamé constants μ	11.25 MPa
	Lamé constants λ	22.5 MPa
	Mass density of the soil ρ	1700 kg m^{-3}
	Visco-elastic constants μ^*	3×10^4 kg m^{-1} s^{-1}
	Visco-elastic constants λ^*	3×10^4 kg m^{-1} s^{-1}
	Poisson's ratio ν	1/3
	Rayleigh wave speed c_R	75.86 m s^{-1}
	Shear wave speed c_S	81.35 m s^{-1}
	Compressive wave speed c_P	162.7 m s^{-1}
Beam	Bending stiffness of the beam EI/a	10^9 N m
	Mass per unit length of the beam ρ_B/a	3×10^4 kg m^{-2}
	Width of beam a	4 m

$$S_p(f) = 1.6 \times 10^9 \text{ N}^2 \text{ Hz}^{-1}, \qquad f \in [0.05, 100] \tag{39}$$

In order to observe the response directly, the random load is assumed to pass through the origin at time $t = 0$.

For verification of the wavelet approach, the integration in Eq. (23) was also carried out by complex Simpson's rule. Table 2 gives the real part of the response magnified 10^7 times, for the chosen parameters $V = 50 \text{ m s}^{-1}$ and $\omega = 4\pi \text{ rad s}^{-1}$ at three time points $0, 0.1, 0.2$ s. In this case, $n = 14$ is sufficient for the wavelet method calculation, but Simpson's rule requires at least 20000 nodes and takes about twice the computation time of the wavelet method. However, as the integrand in Eq. (23) is highly oscillatory at some frequencies and velocities, the wavelet method has some clear advantages. A series of numerical experiments showed that $n = 17$ gives adequate precision in an acceptable computation time.

Table 2
Comparison of numerical results and computational time between two methods

Method	Amount of calculation	Response			Computational time
		$t = 0$ s	$t = 0.1$ s	$t = 0.2$ s	
Complex Simpson's rule	10k nodes	-0.15564	-0.10967	-0.08971	0.045s
	20k nodes	-0.15553	-0.10854	-0.08854	0.094s
	30k nodes	-0.15532	-0.10852	-0.08851	0.132s
Wavelet method	$n = 13$	-0.15527	-0.10871	-0.08868	0.028s
	$n = 14$	-0.15532	-0.10851	-0.08851	0.056s
	$n = 15$	-0.15532	-0.10851	-0.08851	0.110s

6.1 Non-stationary PSD of vertical displacement

The non-stationary PSD of vertical displacement at the origin is shown in Figure 3. The numerical results show that the load velocity is the key factor determining the frequency at which the PSD takes its maximum value. The properties of the PSD are described in three stages which are dependent on the load velocity.

Stage 1: $V \leq 100\, m\, s^{-1}$. Two peaks emerge immediately after the load has passed through the origin. The first peak is sharp at very low frequencies and is in a dominant position, whilst the second peak is relatively insignificant and is smooth over a range of frequencies. If the viscous damping is not taken into account, the integrand in Eq. (23) can be taken as a first order singular function determined by load

velocity V, frequency f and wavenumber θ. For a given load velocity, the numerical integration can be executed at frequencies where the singularity does not occur. However, the viscous damping dramatically weakens the singularity. The response calculated by the wavelet method shows some properties of a step function, but it truly reflects the resonance of the system at these frequencies. Before the load reaches the origin, the response at each frequency is rather flat, but afterwards the response at low frequencies clearly fluctuates.

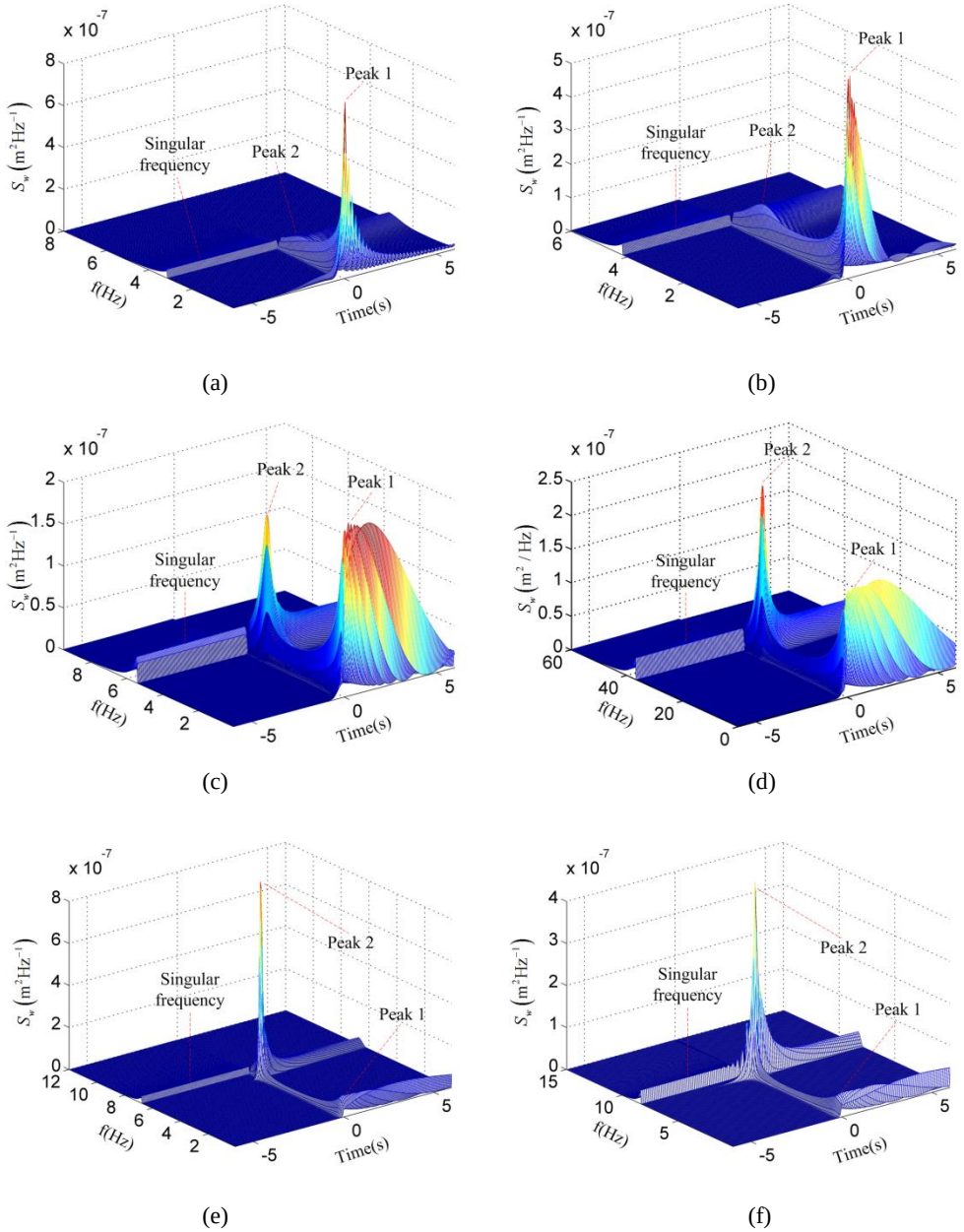

Figure 3. Non-stationary PSD of vertical displacement at the origin:
(a) $V = 75.86\ \mathrm{m\ s^{-1}}$, (b) $V = 100\ \mathrm{m\ s^{-1}}$, (c) $V = 130\ \mathrm{m\ s^{-1}}$,
(d) $V = 140\ \mathrm{m\ s^{-1}}$, (e) $V = 162.7\ \mathrm{m\ s^{-1}}$, (f) $V = 200\ \mathrm{m\ s^{-1}}$.

Stage 2: $100\ m\ s^{-1} < V \leq 140\ m\ s^{-1}$. With increasing load velocity, the second peak in stage 1 grows rapidly and drifts to higher frequencies, whilst the first peak becomes smoother and lasts longer on the time axis. The second peak has a tendency to exceed the first peak, but no matter which one is larger, they both play an important role in shaping the response.

Stage 3: $V > 140\ m\ s^{-1}$. The second peak in this stage is in a dominant position, like the first peak in stage 1. After the load has passed the origin, the response remains at very low frequencies for quite a long time. With increasing load velocity the PSD continues to drift to higher frequencies; the frequency band where the second peak occurs becomes narrower; at the same time some fluctuation arises around the peak.

6.2 Time-dependent standard deviation

Figure 4 shows the standard deviation of vertical displacement at the origin. Meanwhile, the response is also computed by a Monte Carlo (MC) method for the verification of the present method. By MC method the load $p(\mathrm{t})$ is regarded as a summation of trigonometric functions

$$p(t) = \sqrt{2}\sum_{k=1}^{N}\sqrt{S_p(\omega_k)\Delta\omega}\cos(\omega_k t + \phi_k) \tag{40}$$

where $S_p(\omega_k)$ is the value of $S_p(\omega)$ at the kth frequency ω_k and $\Delta\omega$ is a discretised small regular interval, ϕ_k is the corresponding phase of ω_k and is taken as a random variable uniformly distributing over the range $[0, 2\pi]$. One thousand samples of ϕ_k are taken to compute the standard deviation. As can be observed in Figure 5, the numerical results from the two methods agree well.

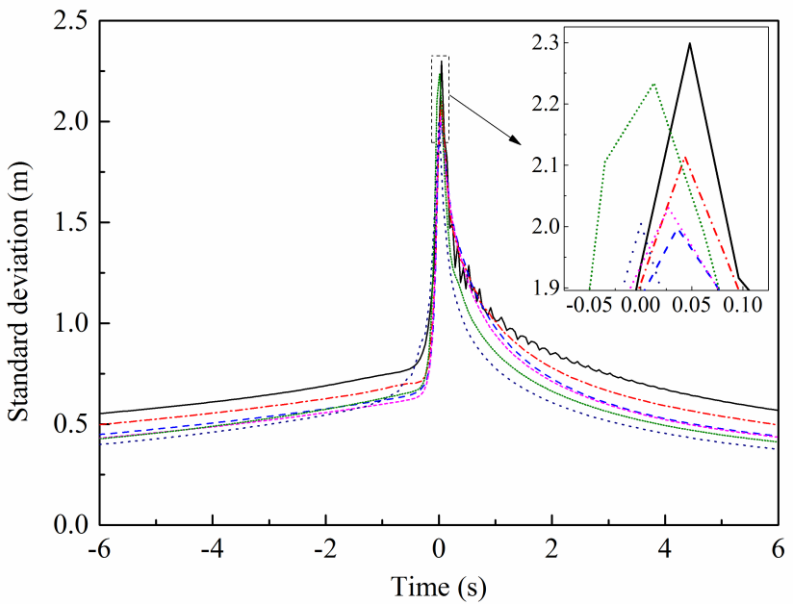

Figure 4. Time-dependent standard deviation of vertical displacement at the origin for six load velocities, solid line $V = 75.86\ \mathrm{m\ s^{-1}}$, dash dot $V = 100\ \mathrm{m\ s^{-1}}$, dashed $V = 130\ \mathrm{m\ s^{-1}}$, short dash $V = 140\ \mathrm{m\ s^{-1}}$, short dot $V = 162.7\ \mathrm{m\ s^{-1}}$, dot $V = 200\ \mathrm{m\ s^{-1}}$.

Due to the visco-elastic behavior of the soil, there is a time delay between the moment when the load passes through the origin and the moment when the deviation achieves its maximum (detailed in the enlargements in Figures 4 and 5). This delay becomes shorter as the load velocity grows larger (as can also be observed in Figure 7). Figure 4 shows that the response attenuates faster with increasing load velocity, the reason being that the energy is shifting to higher frequencies and hence the viscous damping can have a more significant influence on the attenuation. The standard deviation tends to be symmetrical with respect to $t = 0$ as the load velocity becomes larger, especially when the load velocity is larger than $200\ \mathrm{m\ s^{-1}}$. When the load velocity is lower than $140\ \mathrm{m\ s^{-1}}$, the amplitude of the peak decreases with increasing load velocity. But when the load velocity is close to $162.7\ \mathrm{m\ s^{-1}}$ (Figure 5(e)), the amplitude significantly increases. To study the mechanism of this phenomenon, a parametric study on critical velocity is made in the following section.

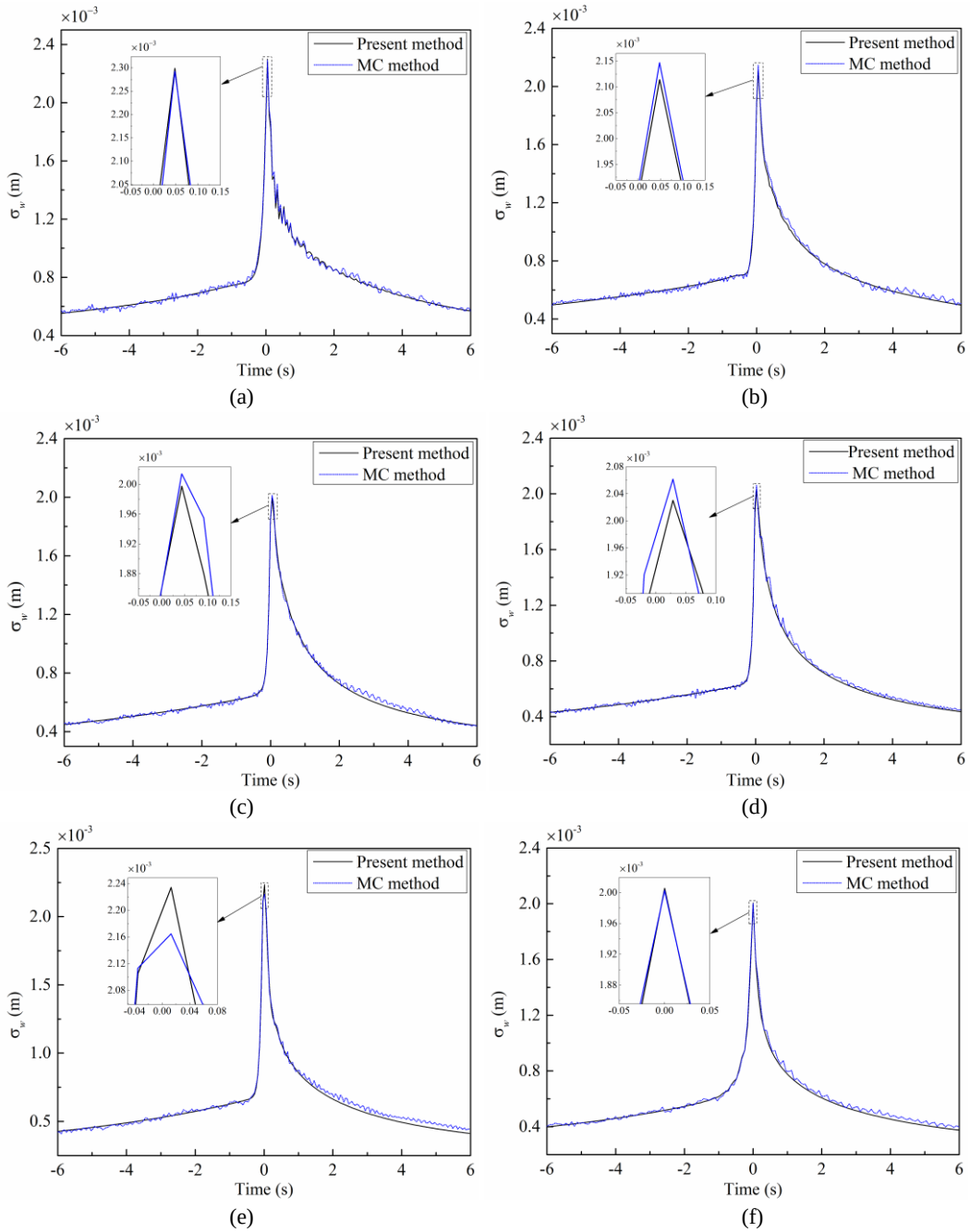

Figure 5. Time-dependent standard deviation of vertical displacement at the origin: (a) $V = 75.86\ \mathrm{m\ s^{-1}}$, (b) $V = 100\ \mathrm{m\ s^{-1}}$, (c) $V = 130\ \mathrm{m\ s^{-1}}$, (d) $V = 140\ \mathrm{m\ s^{-1}}$, (e) $V = 162.7\ \mathrm{m\ s^{-1}}$, (f) $V = 200\ \mathrm{m\ s^{-1}}$.

6.3 Parametric study on critical velocity

It is well known that if a half-space is subjected to a moving constant load, the critical velocity of the system is almost equal to the Rayleigh wave velocity. For ground vibration induced by a moving harmonic load, Dieterman and Metrikine [43] determined the critical velocities of a constant load moving at constant speed along an Euler-Bernoulli beam by obtaining the equivalent stiffness of an elastic half-space,

which depends on the frequency and the wavenumber of the waves in the beam. References [15, 21] show that for a track-soil structure, there exists a wave in the track-soil system whose velocity is lower than the velocity of lowest propagating wave in the layered ground structure. For a beam-soil structure under a moving random load, it can be reasonably assumed that the response's maximum PSD is determined simultaneously by the characteristics of both the beam and the soil. Although a load moving near the Rayleigh wave velocity can cause the response's PSD to have maximum values at some frequencies (Figure 3(a)), the standard deviation obtained by integration of the PSD (Eq. (25)) in the frequency domain may not dominate the maximum value mentioned above (Figure (5a)), because the standard deviation reflects the energy over the whole frequency range. Here a parametric study is made to analyse which velocity gives the critical deviation. Also an analysis is performed to indicate that the critical velocity is an inherent property of the beam-soil structure.

6.3.1 Influence of viscous damping on critical velocity

Curves of the maximum standard deviations of vertical displacement at the origin against velocity for three viscous damping cases are shown in Figure 6. The corresponding time delay, i.e. the time difference between the moment the load passes through the origin and the moment the standard deviation achieves its maximum, are shown in Figure 7. As shown in Figure 6, the viscous damping has insignificant influence when the load velocity is less than $125\ \mathrm{m\,s^{-1}}$. But when the load velocity is near to $170\ \mathrm{m\,s^{-1}}$, the standard deviation is obviously sensitive to the viscous damping. At higher load velocities the response decreases rapidly. Note that the location of maximum standard deviation does not vary with different viscous damping cases, and it can initially be assumed that for the beam-soil structure subjected to a moving random load the critical velocity is close to the dilatational velocity of the soil. Also, it can be assumed that the response maintains a high value before the load velocity reaches $50\ \mathrm{m\,s^{-1}}$ (lower than the Rayleigh wave speed), also due to the properties of the beam and the soil.

As has been discussed in section 6.2, the time delay becomes shorter as the velocity grows (Figure (7)). When the time delay becomes very small, one can regard the standard deviation as approximately symmetrical with respect to $t = 0$ (Figure

5(f)). Different viscous damping has no obvious influence on time delay, but it can obviously change the response amplitude, especially when the load velocity is near the dilatational wave velocity.

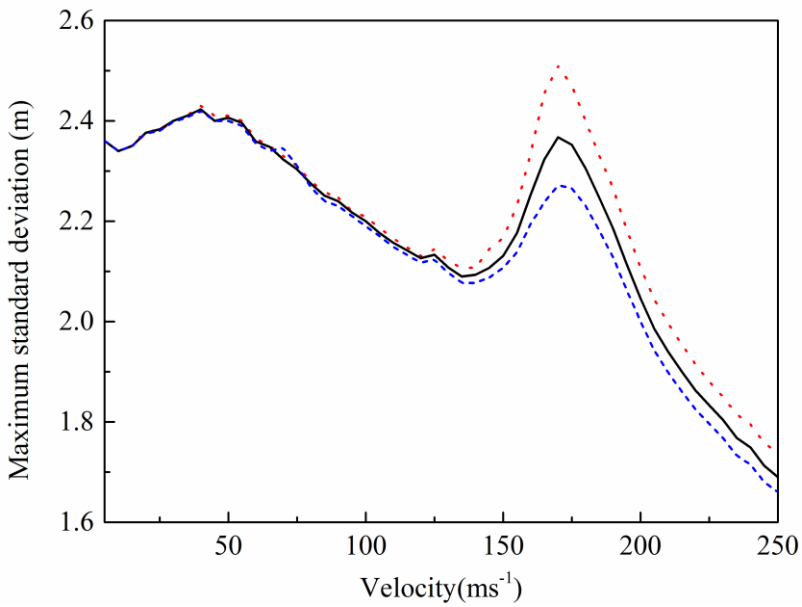

Figure 6. Maximum standard deviation of vertical displacement versus load velocity at the origin for three viscous damping cases, dot-line $\lambda^* = \mu^* = 2 \times 10^4$ kg m^{-1} s^{-1}, solid $\lambda^* = \mu^* = 3 \times 10^4$ kg m^{-1} s^{-1}, short dash $\lambda^* = \mu^* = 4 \times 10^4$ kg m^{-1} s^{-1}.

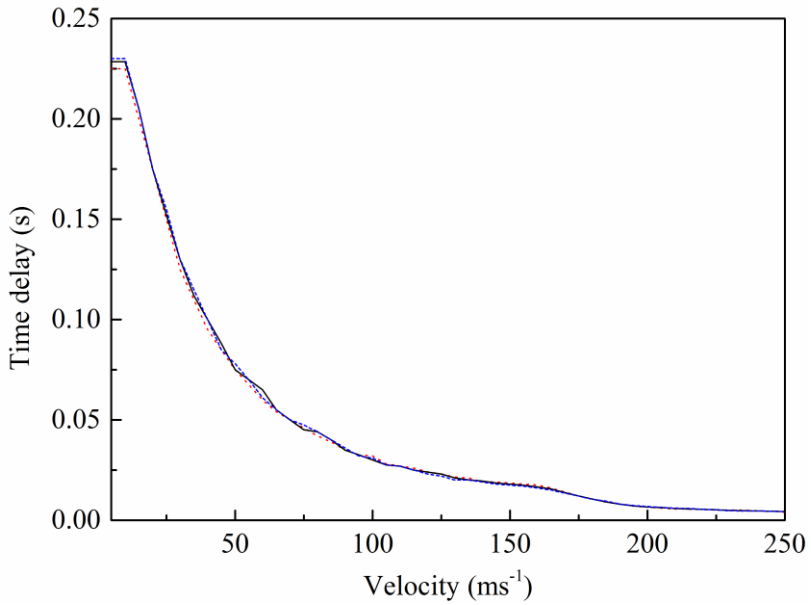

Figure 7. Corresponding time delay versus load velocity for three viscous damping cases, dot-line $\lambda^* = \mu^* = 2 \times 10^4$ kg m^{-1} s^{-1}, solid $\lambda^* = \mu^* = 3 \times 10^4$ kg m^{-1} s^{-1}, short dash $\lambda^* = \mu^* = 4 \times 10^4$ kg m^{-1} s^{-1}.

6.3.2 Influence of elastic modulus on critical velocity

To validate the proposition, the maximum standard deviations of vertical displacement at the origin against velocity are shown in Figure 8 for three different soils, and their corresponding time delays are shown in Figure 9. Some parameters for the soils are shown in Table 3, while the other parameters including soil density, Poisson's ratio and visco-elastic constants are shown in Table 1.

Table 3

Parameters for different soils

Soils	Soil A	Soil B	Soil C
Elastic modulus	20 MPa	30 MPa	40 MPa
Lamé constants μ	7.5 MPa	11.25 MPa	15 MPa
Lamé constants λ	15 MPa	22.5 MPa	30 MPa
Rayleigh wave speed	61.94 m s^{-1}	75.86 m s^{-1}	87.6 m s^{-1}
Shear wave speed	66.42 m s^{-1}	81.35 m s^{-1}	93.93 m s^{-1}
Compressive wave speed	132.84 m s^{-1}	162.7 m s^{-1}	187.87 m s^{-1}

Obviously, at the same load velocity, softer soils have a larger response. The critical velocities for the three soils are $153\ \mathrm{m\ s^{-1}}$, $170\ \mathrm{m\ s^{-1}}$ and $185\ \mathrm{m\ s^{-1}}$, respectively. As the soil becomes harder, the critical velocities become closer to their compressive wave speeds. This indicates that the influence of the beam on the critical velocity is weakened for harder soil. So for a beam-soil structure under a moving random load, especially if the soil is hard, it is reasonable to take the compressive wave speed as the critical velocity. However, the fact that the response has a high value in low velocity ranges (smaller than the Rayleigh wave speed) should also be noted.

Although the time delay is induced by the viscous damping, it is more sensitive to the elastic modulus (Figure 9). Before the load velocity reaches $153\ \mathrm{m\ s^{-1}}$, softer soil causes a larger delay. The time delay decreases quickly when the load velocity is below $50\ \mathrm{m\ s^{-1}}$, and after that it decreases more slowly, especially when the load velocity is larger than the critical velocity.

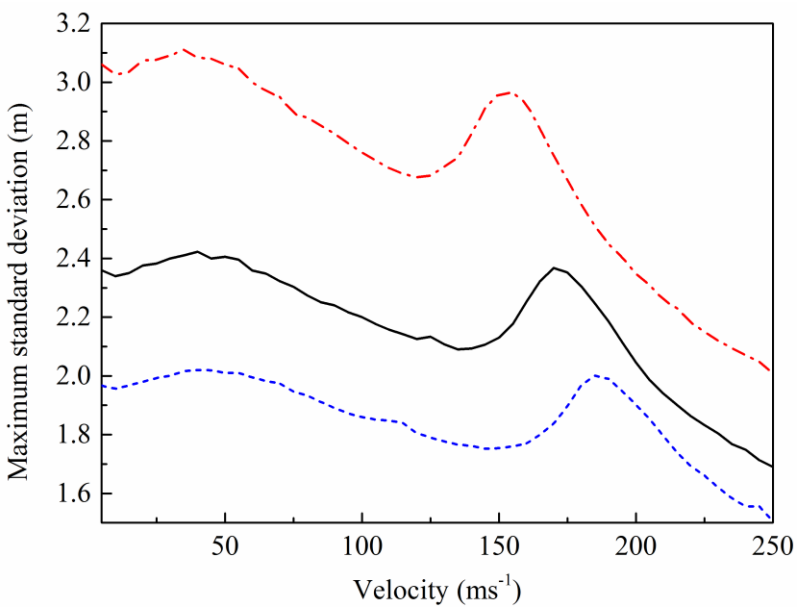

Figure 8. Maximum standard deviation of vertical displacement versus load velocity at the origin for different soils, dash dot-line soil A, solid soil B, short dash soil C.

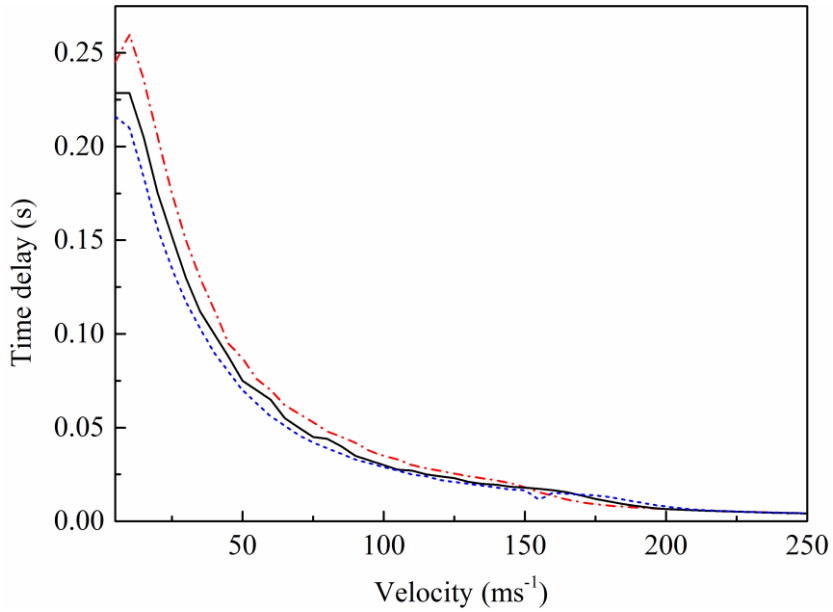

Figure 9. Correspondingly time delay versus load velocity for different soils, dash dot-line soil A , solid soil B, short dash soil C.

However, to evaluate ground vibration induced by trains, the model is far from reality. Besides, the PSD of the moving load is represented by a band-limited white noise, which has the same value at different velocities and frequencies. To obtain

more realistic results, one has to consider a detailed three-dimensional model. Nonetheless, the response obtained can provide a useful guide to estimate the ground vibration caused by traffic loads.

7. Conclusions

The stochastic vibration analysis of a beam-soil structure subjected to a moving random load has been studied. Based on the pseudo-excitation method, analytical solutions for the non-stationary power spectral density and standard deviation of vertical displacement are derived in integral form. A wavelet approach is introduced to calculate the integrand. Numerical results for the power spectral density locate the major frequency band at which large vibrations occur at different load velocities. The plots of standard deviation against time show the general trend of vibration, while the maximum standard deviations indicate the velocities worthy of attention. Furthermore, a parametric study is made to study the mechanism of the critical velocity of the system. The hybrid method presents a practical and efficient approach for studying the random responses of beam-soil structures subjected to moving random loads.

Acknowledgements

The authors are grateful for support under grants from the National Basic Research Program of China (2014CB046803) and the Fundamental Research Funds for the Central Universities (DUT15TD34).

References

[1] H. Lamb, On the Propagation of Tremors over the Surface of an Elastic Solid, *Philosophical Transactions of the Royal Society A: Mathematical, Physical and Engineering Sciences* 203 (1904) 1-42.

[2] G. Eason, The stresses produced in a semi-infinite solid by a moving surface force, *International Journal of Engineering Science* 2 (1965) 581-609.

[3] D.C. Gakenheimer, J. Miklowitz, Transient excitation of an elastic half space by a point load traveling on the surface, *Journal of Applied Mechanics* 36 (1969) 505-515.

[4] L. Fryba, Vibration of solids and structures under moving loads, Groningen, The Netherlands: Noordhoff International Publishing, (1972).

[5] V. Krylov, C. Ferguson, Calculation of Low-Frequency Ground Vibrations from Railway Trains, *Applied Acoustics* 42 (1994) 199-213.

[6] V. Krylov, Generation of Ground Vibrations by Superfast Trains, *Applied Acoustics* 44 (1995) 149-164.

[7] H. Takemiya, K. Goda, Prediction of ground vibration induced by high-speed train

operation, in: Proceedings of the 18th Sino-Japan Technology Seminar, (1997) 1-10.
[8] M. Gunaratne, O. Sanders, Response of a layered elastic medium to a moving strip load, *International Journal for Numerical and Analytical Methods in Geomechanics* 20 (1996) 191-208.
[9] D.V. Jones, D. Le Houedec, A.T. Peplow, M. Petyt, Ground vibration in the vicinity of a moving harmonic rectangular load on a half-space, *European Journal of Mechanics A/Solids* 17 (1998) 153-166.
[10] D.V. Jones, D. Le Houedec, M. Petyt, Ground vibrations due to a rectangular harmonic load, *Journal of Sound and Vibration* 212 (1998) 61-74.
[11] G. Lefeuve-Mesgouez, D. Le Houedec, A.T. Peplow, Ground vibration in the vicinity of a high-speed moving harmonic strip load, *Journal of Sound and Vibration* 231 (2000) 1289-1309.
[12] G. Lefeuve-Mesgouez, A.T. Peplow, D. Le Houedec, Surface vibration due to a sequence of high speed moving harmonic rectangular loads, *Soil Dynamics and Earthquake Engineering* 22 (2002) 459-473.
[13] H.H. Hung, Y.B. Yang, Elastic waves in visco-elastic half-space generated by various vehicle loads, *Soil Dynamics and Earthquake Engineering* 21 (2001) 1-17.
[14] X. Sheng, C.J.C. Jones, M. Petyt, Ground vibration generated by a harmonic load acting on a railway track, *Journal of Sound and Vibration* 225 (1999) 3-28.
[15] X. Sheng, C.J.C. Jones, M. Petyt, Ground vibration generated by a load moving along a railway track, *Journal of Sound and Vibration* 228 (1999) 129-156.
[16] C.J.C. Jones, X. Sheng, M. Petyt, Simulations of ground vibration from a moving harmonic load on a railway track, *Journal of Sound and Vibration* 231 (2000) 739-751.
[17] H.E.M. Hunt, Stochastic modelling of traffic-induced ground vibration, *Journal of Sound and Vibration* 144 (1991) 53-70.
[18] H.E.M. Hunt, Modelling of road vehicles for calculation of traffic-induced ground vibration as a random process, *Journal of Sound and Vibration* 144 (1991) 41-51.
[19] L. Sun, B.S. Greenberg, Dynamic response of linear systems to moving stochastic sources, *Journal of Sound and Vibration* 229 (2000) 957-972.
[20] A. Metrikine, A. Vrouwenvelder, Surface ground vibration due to a moving train in a tunnel: two-dimensional model, *Journal of Sound and Vibration* 234 (2000) 43-66.
[21] X. Sheng, C. Jones, D. Thompson, A theoretical model for ground vibration from trains generated by vertical track irregularities, *Journal of Sound and Vibration* 272 (2004) 937-965.
[22] F. Lu, Q. Gao, J. Lin, F. Williams, Non-stationary random ground vibration due to loads moving along a railway track, *Journal of Sound and Vibration* 298 (2006) 30-42.
[23] G. Lombaert, G. Degrande, Ground-borne vibration due to static and dynamic axle loads of InterCity and high-speed trains, *Journal of Sound and Vibration* 319

(2009) 1036-1066.
[24] G. Lombaert, G. Degrande, D. Clouteau, The non-stationary freefield response for a moving load with a random amplitude, *Journal of Sound and Vibration* 297 (2004) 611-635.
[25] G. Lombaert, G. Degrande, D. Clouteau, Numerical modelling of free field traffic-induced vibrations, *Soil Dynamics and Earthquake Engineering* 19 (2000) 473-488.
[26] G. Lombaert, G. Degrande, J. Kogut, S. Francois, The experimental validation of a numerical model for the prediction of railway induced vibrations, *Journal of Sound and Vibration* 297 (2006) 512-535.
[27] J.H. Lin, Y. Zhao, Y.H. Zhang, Accurate and highly efficient algorithms for structural stationary/non-stationary random responses, *Computer Methods in Applied Mechanics and Engineering* 191 (2001) 103-111.
[28] J.H. Lin, Y.H. Zhang, Y. Zhao, *Seismic random response analysis*, Bridge Engineering Handbook (2014) 133-162.
[29] Y.W. Zhang, J.H. Lin, Y. Zhao, W.P. Howson, F.W. Williams. Symplectic random vibration analysis of a vehicle moving on an infinitely long periodic track, *Journal of Sound and Vibration* 329 (2010) 4440-4454.
[30] K. Knothe, S.L. Grassie, Modelling of railway track and vehicle/track interaction at high frequencies, Vehicle Systems Dynamics 22 (1993) 209–262.
[31] J.C.O. Nielsen, A. Igeland, Vertical dynamic interaction between train and track-influence of wheel and rail imperfections, *Journal of Sound and Vibration* 187(5) (1995) 825–839.
[32] J. Wang, Y. Zhou, H. Gao, Computation of the Laplace inverse transform by application of the wavelet theory, *Communications in Numerical Methods in Engineering* 19 (2003) 959-975.
[33] Y. Meyer, *Wavelets and Operators*, Cambridge University Press, Cambridge, 1992.
[34] G. Beylkin, R. Coifman, V. Rokhlin, Fast wavelet transforms and numerical algorithms, *Communications on Pure and Applied Mathematics* 44 (1991) 141-183.
[35] L. Monzón, G. Beylkin, Compactly supported wavelets based on almost interpolating and nearly linear phase filters (Coiflets), *Applied and Computational Harmonic Analysis* 7 (1999) 184-210.
[36] M. Lieb, B. Sudret, A fast algorithm for soil dynamics calculations by wavelet decomposition, *Archive of Applied Mechanics* 68 (1998) 147-157.
[37] H. Grundmann, M. Lieb, E. Trommer, The response of a layered half-space to traffic loads moving along its surface, *Archive of Applied Mechanics* 69 (1999) 55-67.
[38] P. Koziol, C. Mares, I. Esat, Wavelet approach to vibratory analysis of surface due to a load moving in the layer, *International Journal of Solids and Structures* 45 (2008) 2140-2159.
[39] P. Koziol, C. Mares, Wavelet approach for vibration analysis of fast moving load on a viscoelastic medium, *Shock and Vibration* 17 (2010) 461-472.

[40] P. Koziol, Z. Hryniewicz, Dynamic response of a beam resting on a nonlinear foundation to a moving load: Coiflet-based solution, *Shock and Vibration* 17 (2012) 995-1007.
[41] Z. Hryniewicz, P. Koziol, Wavelet-based solution for vibrations of a beam on a nonlinear viscoelastic foundation due to moving load, *Journal of Theoretical and Applied Mechanics* 51 (2013) 215-224.
[42] P. Koziol, Wavelet approximation of Adomian's decomposition applied to the nonlinear problem of a double-beam response subject to a series of moving loads, *Journal of Theoretical and Applied Mechanics* 52 (2014) 687-697.
[43] H. A. Dieterman, A. Metrikine, The equivalent stiffness of a half-space interacting with a beam. Critical velocities of a moving load moving along the beam, *European Journal of Mechanics. A-Solids* 15 (1996) 67-90.

Appendix: Low pass coiflet filter coefficients p_k

-0.002392638657280051	-0.004932601854180402	0.02714039971139949
0.03064755594619984	-0.1393102370707997	-0.08060653071779983
0.6459945432939942	1.116266213257999	0.5381890557079980
-0.09961543386239989	-0.07992313943479994	0.05149146293240031
0.01238869565706006	-0.01583178039255944	-0.002717178600539990
0.002886948664020020	0.0006304993947079994	-0.0003058339735960013

Figure captions

Figure 1. Beam-soil structure under a moving random load.

Figure 2. Flow chart of the hybrid method.

Figure 3. Non-stationary PSD of vertical displacement at the origin:

(a) $V = 75.86\ \mathrm{m\ s^{-1}}$, (b) $V = 100\ \mathrm{m\ s^{-1}}$, (c) $V = 130\ \mathrm{m\ s^{-1}}$,

(d) $V = 140\ \mathrm{m\ s^{-1}}$, (e) $V = 162.7\ \mathrm{m\ s^{-1}}$, (f) $V = 200\ \mathrm{m\ s^{-1}}$.

Figure 4. Time-dependent standard deviation of vertical displacement at the origin for six load velocities, solid line $V = 75.86\ \mathrm{m\ s^{-1}}$, dash dot $V = 100\ \mathrm{m\ s^{-1}}$, dashed $V = 130\ \mathrm{m\ s^{-1}}$, short dash $V = 140\ \mathrm{m\ s^{-1}}$, short dot $V = 162.7\ \mathrm{m\ s^{-1}}$, dot $V = 200\ \mathrm{m\ s^{-1}}$.

Figure 5. Time-dependent standard deviation of vertical displacement at the origin:

(a) $V = 75.86\ \mathrm{m\ s^{-1}}$, (b) $V = 100\ \mathrm{m\ s^{-1}}$, (c) $V = 130\ \mathrm{m\ s^{-1}}$,

(d) $V = 140\ \mathrm{m\ s^{-1}}$, (e) $V = 162.7\ \mathrm{m\ s^{-1}}$, (f) $V = 200\ \mathrm{m\ s^{-1}}$.

Figure 6. Maximum standard deviation of vertical displacement versus load velocity at the origin for three viscous damping cases, dot-line $\lambda^* = \mu^* = 2 \times 10^4\ \mathrm{kg\ m^{-1}\ s^{-1}}$, solid $\lambda^* = \mu^* = 3 \times 10^4\ \mathrm{kg\ m^{-1}\ s^{-1}}$, short dash $\lambda^* = \mu^* = 4 \times 10^4\ \mathrm{kg\ m^{-1}\ s^{-1}}$.

Figure 7. Corresponding time delay versus load velocity for three viscous damping cases, dot-line $\lambda^* = \mu^* = 2 \times 10^4\ \mathrm{kg\ m^{-1}\ s^{-1}}$, solid $\lambda^* = \mu^* = 3 \times 10^4\ \mathrm{kg\ m^{-1}\ s^{-1}}$, short dash $\lambda^* = \mu^* = 4 \times 10^4\ \mathrm{kg\ m^{-1}\ s^{-1}}$.

Figure 8. Maximum standard deviation of vertical displacement versus load velocity at the origin for different soils, dash dot-line soil A, solid soil B, short dash soil C.

Figure 9. Correspondingly time delay versus load velocity for different soils, dash dot-line soil A , solid soil B, short dash soil C.

Table captions

Table 1 Parameters of the system

Table 2 Comparison of numerical results and computational time between two methods

Table 3 Parameters for different soils